ELSEVIER

Surface Science 376 (1997) 13–31

surface science

Strain mediated two-dimensional growth kinetics in metal heteroepitaxy: Ag/Pt(111)

Holger Röder, Karsten Bromann, Harald Brune *, Klaus Kern

Institut de Physique Expérimentale, EPF Lausanne, CH-1015 Lausanne, Switzerland

Received 8 July 1996; accepted for publication 27 November 1996

Abstract

We have investigated the influence of strain on the morphology in metal heteroepitaxy at temperatures where growth is dominated by kinetics. Whereas Ag(111) homoepitaxy is three dimensional below 400 K, the growth of Ag on Pt(111) proceeds two dimensionally up to a critical film thickness after which a transition to 3D growth is observed. This critical thickness increases from 1 ML at 130 K to 6–9 ML at 300 K. It is demonstrated that the 2D growth in the heteroepitaxial system is due to the particular growth kinetics induced by the compressive strain of the Ag films. The strained Ag layers are found to have substantially lower activation barriers for interlayer mass transport compared to strain free Ag(111). Further, strain and its relief in dislocations also lead to layer-dependent nucleation densities. Both these effects strongly promote layer-by-layer growth. The transition to 3D growth is triggered by the structural transition from strained Ag layers to a perfect Ag(111) termination. It is generally expected that compressive strain promotes 2D growth.

Keywords: Additional step edge barrier; Epitaxy; Growth kinetics; Pin holes; Platinum; Scanning tunneling microscopy; Silver; Strain

1. Introduction

Molecular beam epitaxy (MBE) is a versatile method for growing thin epitaxial films with monolayer precision. Its ultimate goal is the controlled fabrication of atomically thin films with smooth abrupt interfaces. In the thermodynamic limit the growth morphology is determined by the balance of the interfacial and surface free energies involved [1,2]. The generally desired layer-by-layer (2D, or Frank–van der Merwe) growth is expected if the wetting condition

$$\Delta\gamma = \gamma_{f,n} + \gamma_{,n} - \gamma_s \leq 0 \qquad (1)$$

is fulfilled independently of the film thickness, where γ_s is the surface free energy of the substrate and $\gamma_{f,n}$, $\gamma_{i,n}$ are the layer-dependent (n = number of layers) surface and interface energies of the film. If on the other hand $\Delta\gamma > 0$ independent of n, three-dimensional clusters nucleate on the bare substrate; a growth scenario which is usually called Volmer–Weber or 3D growth. In many cases of heteroepitaxial growth $\Delta\gamma$ is found to be negative for the first few monolayers before, at a critical layer thickness n^*, $\Delta\gamma$ becomes positive and the growth changes from 2D to 3D. This growth mode is usually called Stranski–Krastanov (SK) growth.

SK growth is believed to be the general thermodynamic growth scenario for heteroepitaxial systems with substantial structural mismatch and small surface energy of the adsorbate. The

* Corresponding author. Fax: +41 21 693 3604; e-mail: harald.brune@ipe.dp.epfl.ch

0039-6028/97/$17.00
PII S0039-6028(96)01336-2

pseudomorphic growth of the first wetting layers results in a strain energy contribution to $\gamma_{f,n}$ and $\gamma_{i,n}$ which increases with layer thickness n, while the negative adhesion contribution due to the substrate strongly decreases with n. Eventually, above a critical layer thickness, the elastic energy stored in the film is too large to allow for continued growth of pseudomorphic layers, and subsequently deposited material collects into islands that have essentially bulk-like structure [3,4]. Usually this transition goes hand in hand with the formation of interfacial misfit dislocations, partially relieving the strain [5]. In the thermodynamic model the onset of strain relief destabilizes layer growth in favor of 3D growth [6,7] and the critical thickness for the coherent–incoherent transition correlates with the layer thickness n^* above which the wetting condition is no longer fulfilled.

In MBE, however, thin films are usually grown under experimental conditions far from equilibrium. Film growth will then be governed by kinetic effects. A link between nucleation kinetics and film morphology is given by the following simple picture. Layer-by-layer growth occurs when stable nuclei start to form on top of islands of the growing layer only *after* these have coalesced. In order to prevent nucleation *before* coalescence, the adatoms landing on top of islands have to be mobile enough to reach their edges at any time during growth which is most difficult at coalescence. Since the island size of the nth layer at coalescence is determined by its saturation island density, which itself is linked to the mobility on the layer underneath (D_{n-1}) the mobility of adatoms on top of the nth layer (D_n) has to be at least D_{n-1} (see Fig. 1). In other words, the *necessary* condition for layer-by-layer growth is that subsequent mobilities obey $D_n \geq D_{n-1}$. Provided this is the case, the *sufficient* condition for layer-by-layer growth is that adatoms are able to descend at island edges. This interlayer diffusion is in general associated with an additional barrier adding to that for terrace diffusion ΔE_s, (or Ehrlich–Schwoebel barrier) encountered by an adatom upon descending a step [8–10].

In homoepitaxial systems, where lattice mismatch is absent, mobilities on subsequent layers are in general identical, i.e. $D_n = D_{n-1}$ [11]. Hence, for a homoepitaxial system, the height of the additional step barrier alone determines the resulting growth morphology. If this barrier is effective at the deposition temperature the system is kinetically limited and grows 3D. If it can be overcome the system is in the thermodynamic limit where a homoepitaxial system always grows 2D, since $\Delta\gamma = 0$ [12]. Notice that the terrace width of the substrate then determines whether step flow or layer-by-layer growth will result, where only the latter gives rise to oscillations of the surface reflectivity. The case of Ag(111) homoepitaxy is an example of this scenario and has been discussed intensively in recent studies [13–16]. It reveals a considerable additional step edge barrier [16–18] and thus

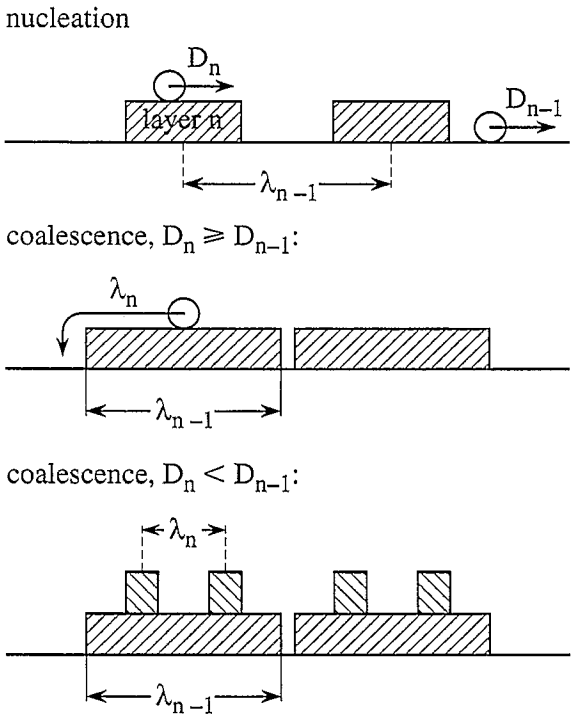

Fig. 1. Model showing the correlation of the growth morphology with diffusitivities, D_n, D_{n-1}, on subsequent layers. The mean island distance λ equals the island diameter at coalescence and is related to the diffusion rate D via the saturation island density n_x by $\lambda_n \propto \sqrt{1/n_x} \propto (D/F^{\chi/2}$, where F is the deposition flux and the exponent χ depends on the size of the critical nucleus [4]. Hence, for $D_n \geq D_{n-1}$ one has $\lambda_n \geq \lambda_{n-1}$, consequently adatoms deposited onto coalescing islands can reach their perimeter which is the necessary condition for layer-by-layer growth, whereas when $D_n \leq D_{n-1}$ islands will nucleate on top of layer n before coalescence, leading to 3D growth.

grows 3D below 400 K and 2D (step flow) at elevated temperatures [13].

The case of Pt(111) homoepitaxy, on the other hand, is an example that reveals microscopic peculiarities which lead to deviations from the simple picture described above [19–21]. At low temperature this system grows 2D since the islands grow ramified and thus provide short diffusion lengths to the edges and enough kink sites at B-type steps ({111}-facets) where the lowest activation energy for interlayer diffusion by exchange is theoretically expected [20]. At 300 K, however, triangular islands with a lack of these particular kink sites form, so that interlayer mass transport is restricted to locations where it requires a higher activation energy, resulting in 3D growth [20]. At temperatures above 400 K the Pt(111) substrate surface reconstructs in the presence of Pt adatoms [22]. This leads to a strongly reduced mobility on the substrate, whereas it remains unchanged on top of the unreconstructed islands, i.e. we have $D_n \gg D_{n-1}$. (The concept of different mobilities on subsequent layers has been introduced for homoepitaxy by Rosenfeld et al. [23].) Together with the fact that the interlayer barrier can readily be overcome at temperatures above 400 K, this causes a rather perfect layer-by-layer growth [21].

The growth kinetics of Pt at high temperature is similar to what generally characterizes heteroepitaxial systems. It has recently been recognized that the strain present in heteroepitaxy significantly alters adatom mobilities. This effect was observed for an isotropically strained psuedomorphic layer [24] as well as for metal layers with strain induced dislocations which also effectively alter diffusion [24,25]. Both effects lead to layer-dependent island densities and in addition, with interlayer diffusion also being modified by strain, to a layer dependence of the overall nucleation kinetics. This behavior can be expected in general for heteroepitaxial systems with non-negligible lattice mismatch.

We will show in the present paper for the example of Ag on Pt(111) (4.3% compressive strain) how this change in nucleation kinetics manifests itself in the growth morphology as a function of layer thickness and temperature. The effect of growth temperature turns out to be very important, since it determines whether and in which way a film of a given thickness can relieve its strain. There is a particularly strong effect of strain on interlayer diffusion. Compressively strained Ag layers are found to have a significantly reduced step edge barrier compared to relaxed Ag(111). In combination with the influence of strain on terrace diffusion we conclude that compressive strain strongly promotes 2D growth. For Ag/Pt this leads to a layer-by-layer growth at relatively low temperatures up to a critical thickness where the system adopts Ag(111) properties. The thickness for this transition increases from 1 ML at 130 K to about 6–9 ML at 300 K. At high temperatures, e.g. 600 K, Ag films again grow perfectly 2D. This is due to thermodynamic reasons and indicates that the difference in surface free energies of Ag(111) and Pt(111) outweighs interface and strain energy contributions. The observed growth morphologies at lower temperatures, however, are of pure kinetic origin.

2. Experimental

The growth experiments were performed in an ultra-high-vacuum system equipped with standard facilities for surface preparation and characterization as well as with a variable-temperature STM (25–800 K) [26,27]. Ag was vapor deposited from an MBE Knudsen cell with a flux of 1.1×10^{-3} ML s^{-1} (one monolayer, 1 ML, refers to the density of the Pt substrate). STM images were recorded in the constant current mode at $V_t = -0.2$ to -1.0 V and $I_t = 0.5$–1.5 nA. In most of the figures the derivative $\partial z/\partial x$ of the lines of constant current was recorded thus representing the surface as it appears when illuminated from left [28]. In other images the gray level corresponds to the height of the lines of constant tunnel current. In order to avoid coarsening of metastable structures, STM images of films grown at low temperature were recorded isothermally to deposition; where growth or annealing have been performed at elevated temperatures (>400 K) the morphology has been imaged at 300 K.

3. Results and discussion

3.1. The effect of strain on interlayer mass transport

The submonolayer growth of Ag on the (111) surfaces of Pt at 130 K and Ag at 110 K are compared in Figs. 2a and 2b, respectively. At these temperatures the mobility of Ag atoms at the island edges is rather limited which results in the aggregation of ramified islands [29,30]. In both systems the pattern shape is dendritic with the characteristic backbones, their orientation being determined by the threefold symmetry of the fcc (111) substrates. The growth in the three $\langle 1\bar{1}2\rangle$-directions is due to the preferred diffusion of one-fold coordinated edge atoms towards the A-type edge ({100} facet) [31]. There is, however, a striking difference between the morphologies which becomes obvious upon closer inspection of Figs. 2a and 2b. Although the islands are quite small in the homoepitaxial case (Fig. 2b) they are frequently covered by second layer islands. In contrast, the Ag aggregates on Pt(111), although much larger, are bare of nuclei on top of them. This even holds for much bigger islands close to coalescence (see Fig. 3a).

This difference can be rationalized using the potential energy diagrams shown in Figs. 2c and 2d. These are based on experimentally determined activation energies for the intra- and interlayer diffusion processes which are in play in the films shown in Figs. 2a and b [16,24]. The barriers for intralayer diffusion on the respective layers have been measured by the variation of saturation island densities with temperature at a critical nucleus size

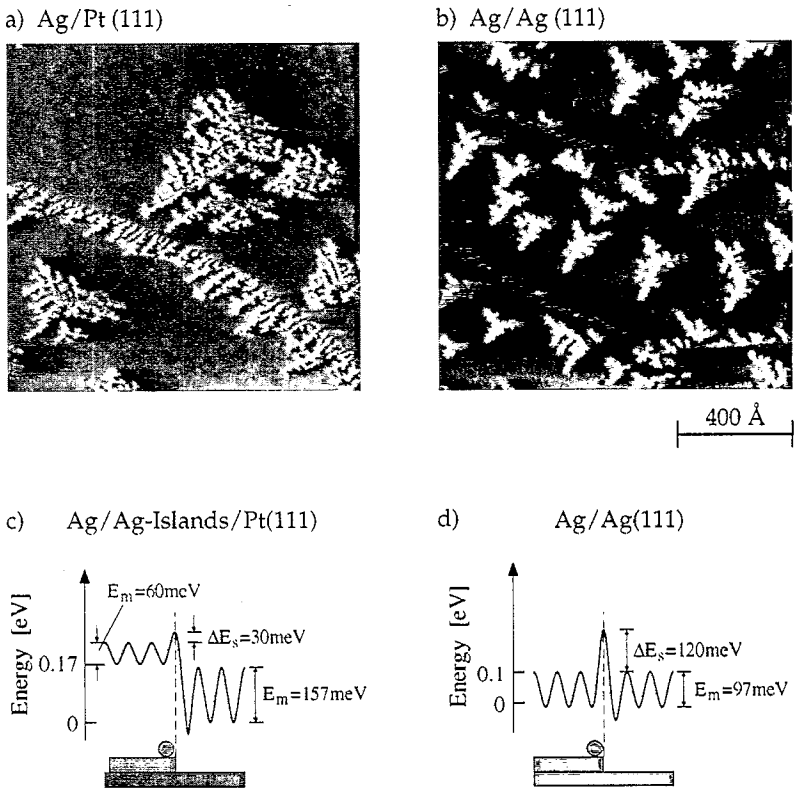

Fig. 2. Dendritic Ag aggregates grown on Pt(111) (a), and on Ag(111) (b), upon deposition of 0.12 ML at 130 K and 110 K, respectively. The potential energy diagrams in (c) and (d) characterize the inter- and intralayer diffusion in Ag heteroepitaxy of the first layer on Pt(111) and in Ag(111) homoepitaxy, respectively. They have been determined by studying the nucleation kinetics on terraces and on top of islands.

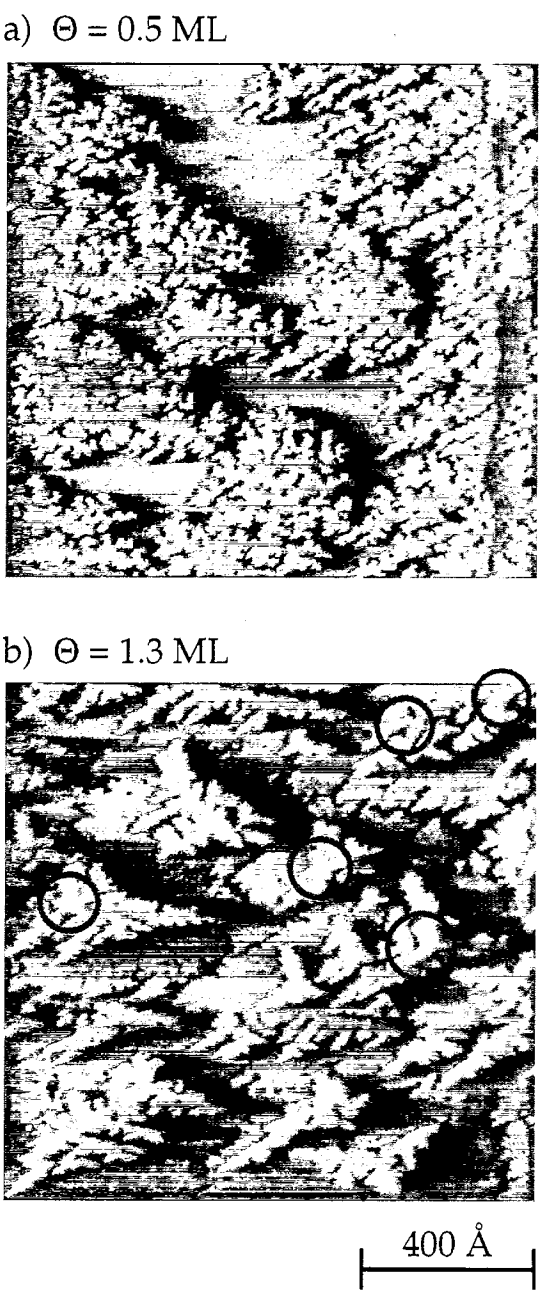

Fig. 3. Morphology of heteroepitaxial Ag films grown on Pt(111) at 130 K; the growth morphology abruptly changes from 2D to 3D above completion of the first monolayer, third layer islands are marked by circles; (a) 0.5 ML and (b) 1.3 ML.

of one and application of mean-field nucleation theory [24,32]. Note the decrease in E_m from 97 ± 10 to 60 ± 10 meV in going from Ag(111) to the first Ag layer on Pt(111). The structure of this layer is pseudomorphic with respect to the Pt(111) substrate [33–35]. Based on calculations within Effective Medium Theory (EMT) this decrease in the surface diffusion barrier has been attributed to the 4.3% compressive strain characterizing the pseudomorphic Ag layer [24]. This interpretation is fully supported by recent ab-initio calculations by Ratsch et al. [36] as well as by Mortensen et al. [37].

The additional step edge barrier has been determined by the nucleation rate of stable islands on top of an island as a function of its size. Tersoff et al. showed that at a critical island radius there is a sharp transition where the nucleation probability on top changes from 0 to 1 [38]. We demonstrated that this sharp transition, when investigated as a function of temperature, can be used to determine ΔE_s with high accuracy [16]. A distribution of circular islands with a size distribution ideally suited for the experiment can be prepared in a simple way via Ostwald ripening. This should render this method applicable for a wide class of epitaxial systems.

For Ag homoepitaxy we obtain an additional step barrier of $\Delta E_s = 120 \pm 15$ meV which is even higher than the Ag adatom diffusion barrier (see Fig. 2d). This explains why, at 110 K, there form second layer nuclei on top of dendritic islands on Ag(111), even though their branches are relatively narrow (see Fig. 2b). It also explains the 3D growth of the homoepitaxial system experimentally observed below 400 K [13]. Large additional step edge barriers for Ag(111) have also been found in previous studies [17,18]. Meyer et al. derived from a linear model of layer occupancies a value of 150 ± 20 meV, which is slightly higher, but within the error margins in agreement with our result. Šmilauer and Harris found 0.19–0.23 eV when comparing the STM data of Meyer et al. to a model based on the critical coverage at the onset of second layer nucleation on top of circular islands. The authors note, however, that this model, in comparison with their KMC simulations, overestimates ΔE_s; they thus regard their results as an

upper limit for ΔE_s [18]. Both evaluations, however, were based on STM data obtained at a single temperature and rely on approximations like equally spaced islands. Therefore they presumably reveal higher uncertainties than the value derived above. Notice that all values discussed here represent an effective barrier which reflects the activation energy for the most efficient interlayer diffusion process, presumably by exchange, and may differ from the barriers for other microscopic sites, as for example straight A-steps where exchange is more difficult.

The additional activation energy for step-down diffusion in the strained heteroepitaxial system Ag/Ag islands/Pt(111) has been determined as 30 ± 5 meV [16], which is only 25% of the barrier in the homoepitaxial case and thus remarkably small. In addition, the migration barrier on top of the first layer is also considerably smaller than that on the Pt(111) surface underneath. Therefore, we have $D_n \gg D_{n-1}$ in combination with a small barrier to interlayer diffusion, which certainly favors 2D growth of the first layer. In agreement, we observe no second layer nucleation up to coverages where the islands have almost coalesced, indicative of almost ideal layer-by-layer growth (see Fig. 3a). The coverage of 0.5 ML short before coalescence is in agreement with the percolation threshold theoretically expected for randomly ramified islands on a hexagonal lattice [39,40]. Notice that for activated interlayer diffusion, percolation will occur at slightly higher coverages than predicted by the models in literature since they only include the material that laterally diffuses towards the islands and neglect atoms that are deposited onto branches and descend from there. In Fig. 3a the compactness of the islands can only be achieved by atoms descending from the branches and thus filling in the free space between them, because this space is effectively screened by the branches from laterally diffusing adatoms.

With the methods outlined above, the potential energy surface for a diffusing Ag adatom could be mapped out on terraces and at descending steps. (The difference in binding energy on the first Ag layer with respect to the Pt substrate was inferred from the desorption temperatures measured in Ref. [33].) With these potentials the low temperature 2D growth of the first Ag layer on Pt(111) and the 3D growth of Ag on Ag(111) are both easily rationalized. The most important reason for the perfect growth of the first Ag layer on Pt is the extremely small value for ΔE_s. We suspect that this lowering is caused by the substantial compressive strain of 4.3% inherent in the first layer [16]. The pseudomorphic islands preferentially relieve their strain at the edges where the Ag atoms are free to expand laterally. This edge relaxation can certainly favor exchange processes, which have been suggested as the mechanism associated with the lowest barrier for atom descent on fcc(111) surfaces [20,41,42]. This strain argument is strongly corroborated by the observation that the low interlayer barrier is only observed where the Ag layer is free to relax at its edge. If this is not the case, e.g. where the Ag layer touches a former Pt step, crossing of this interface is inhibited leading to the formation of pin holes as discussed in more detail below.

3.2. Transition to 3D growth and interlayer diffusion from the second layer

For thicker films on Pt(111) at 130 K, the growth morphology abruptly changes from 2D to 3D above completion of the first monolayer (Fig. 3b). At 1.3 ML the first layer is almost completed and the nucleated second layer islands again exhibit a ramified dendritic structure, indicating that the same mechanism of ramification in preferred directions is also operative for islands on the first layer [31]. In contrast to the first monolayer, the third layer nucleates even on small second layer islands (see circles). The populations of the second and third layers are quite similar to that of Ag(111) shown in Fig. 2b. Diffraction measurements in fact reveal that the 3D islands growing on the pseudomorphic monolayer at low temperature are Ag(111) crystallites with essentially the Ag bulk lattice constant [43]. The transition from 2D to 3D growth is thus associated with a transition in structure from strained pseudomorphic to relaxed Ag(111)-like films. An increase of ΔE_s from the fully strained case (30 meV) towards the Ag(111) value (120 meV) accompanies this transition and hence growth proceeds 3D.

This transition from 2D to 3D growth after one

layer is also seen at 170 K. At this temperature the mean free path of Ag adatoms on Pt(111) approaches the average terrace width of 1000 Å. This results in almost perfect step flow growth (in Fig. 4a there is only one small island that nucleated on the first layer at a coverage of 0.6 ML). At 1.1 ML, Fig. 4b, small islands of the second layer nucleate preferentially where the first Ag layer touches the former Pt step. As for growth at 130 K, third layer nucleation immediately sets in on these islands (see small bright spots on the second layer islands). The image in Fig. 4c shows that at 2.1 ML 15% of the first layer is still visible while the fourth layer starts to nucleate, leading to four simultaneously open layers. Notice that former substrate steps are easily recognized, since islands, even in higher layers, stop growing there [44]. This effect will be discussed in more detail below.

The growth scenario changes again at higher temperatures. The film growth at 200 K is shown in Fig. 5. The 2D step flow growth, seen at 170 K only for the first layer, continues here in the second monolayer up to about 1.7 ML (at 170 K third layer nucleation starts at 1.1 ML). At this coverage the second layer reaches the critical size to nucleate islands on top (Fig. 5a). Films thicker than 2 ML grow 3D as can be seen by the evolution of growth pyramids in Figs. 5b and 5c. After deposition of 2.7 ML Ag, 5 layers are found to be exposed simultaneously and at a coverage of 3.9 ML as many as 7 monolayers are uncovered. A quantitative analysis of the interlayer mass transport is possible from the histograms of uncovered layers shown on the right hand side of Fig. 5. It is known that ideal 3D growth with no interlayer mass transport is characterized by a Poisson distribution of the visible fraction A_n of layers n, $A_n = (\Theta^n/n!)\exp(-\Theta)$. The histograms of the visible frac-

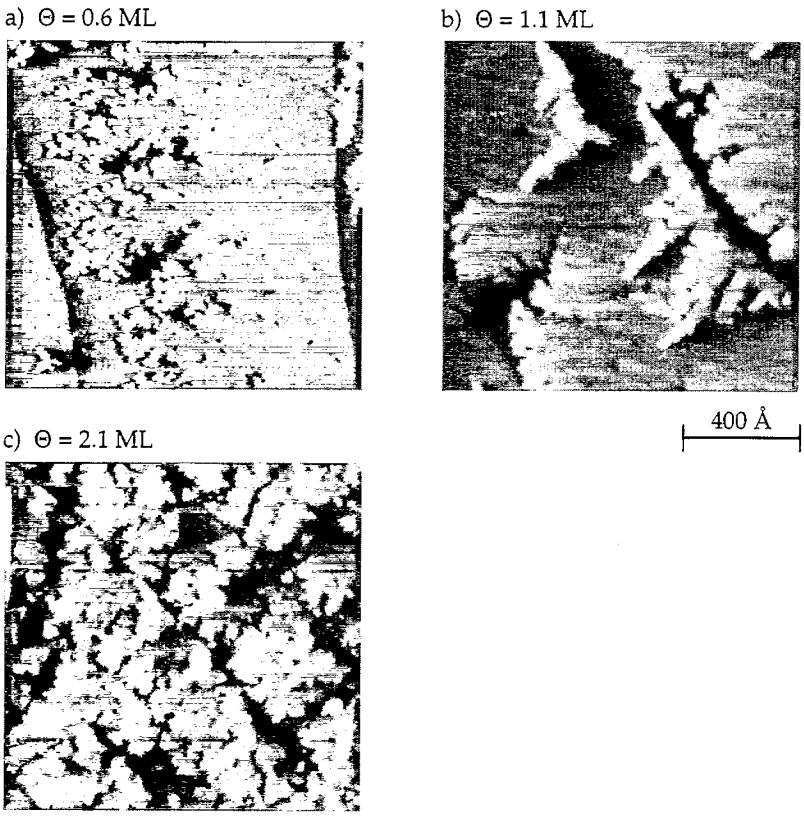

Fig. 4. Growth morphology of Ag on Pt(111) at 170 K; (a) 0.6 ML, (b) 1.1 ML, (c) 2.1 ML.

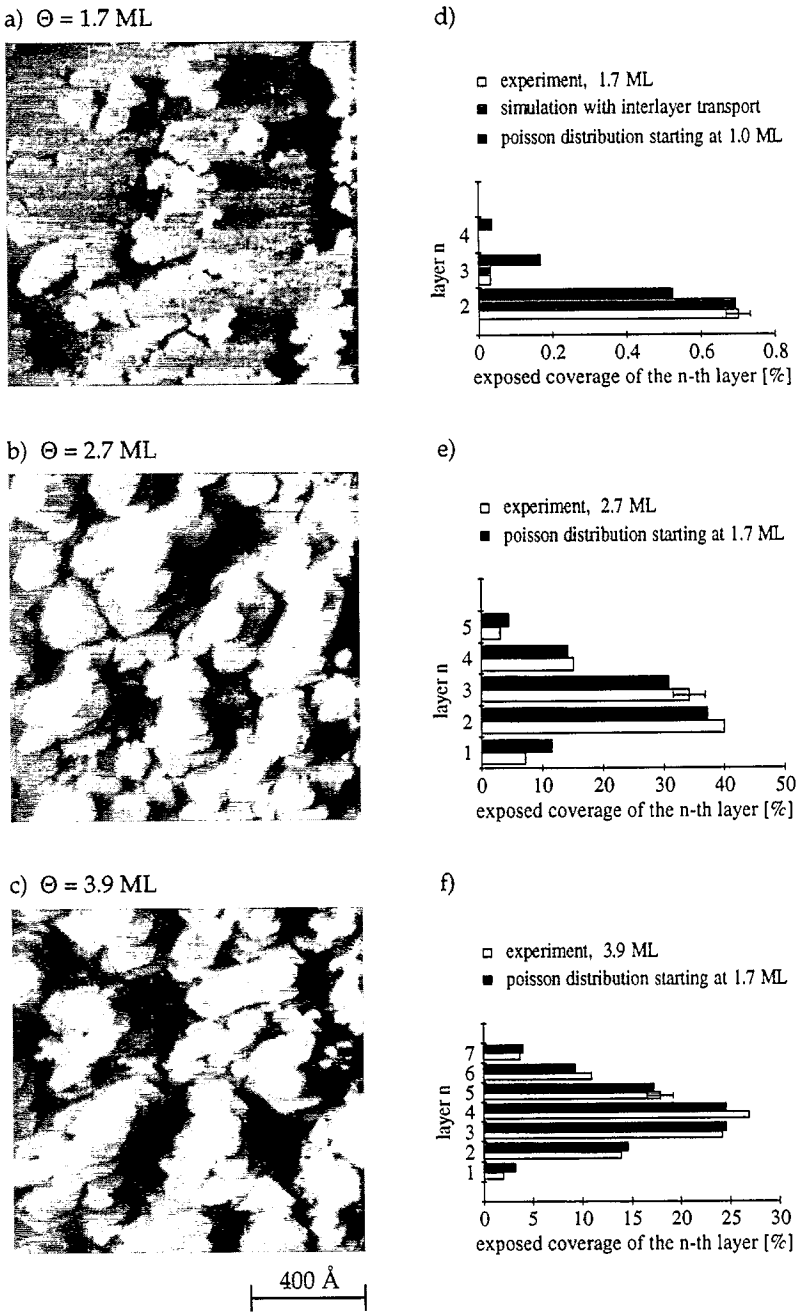

Fig. 5. Heteroepitaxial growth of Ag on Pt(111) at 200 K. Left hand side: STM images characterizing the morphologies of (a) 1.7 ML, (b) 2.7 ML and (c) 3.9 ML thick Ag films. Right hand side: fractions of open layers $\Theta_n - \Theta_{n+1}$ as obtained from STM images, compared to calculated Poisson distributions; the histogram in (d) includes results from a model accounting for interlayer mass transport from the second to the first layer.

tion of the nth layer for the 2.7 ML and 3.9 ML thick Ag films exactly obey these Poisson statistics. In the calculated distributions the 2D growth up to 1.7 ML has been taken into account by starting the Poisson distribution at that coverage. Consequently, there is negligible downward mass transport after three monolayers at 200 K. This 3D growth of thicker films indicates a step edge barrier close to the value for Ag homoepitaxial growth beyond the third monolayer.

There is, however, appreciable mass transport from on top of the second monolayer down onto the first which mediates a quasi-2D growth of the second Ag layer at 200 K. Accordingly, the measured layer histogram of the 1.7 ML film shows significant deviations from a Poisson distribution started at 1.0 ML. We can use the measured layer occupation to estimate the additional step edge barrier for a third layer Ag adatom to step down and attach to second Ag layer at 200 K. For this purpose we apply a linear interlayer mass transport model similar to that of Cohen et al. [45]. In recent literature, this model has been modified in order to account for layer-dependent interlayer [13] and also intralayer diffusivity [17,18]. In these models, interlayer diffusion is described by a parameter λ_n, which denotes the fraction of atoms which diffuse downward from layer n and subsequently attach to it. In our case it can be assumed for simplicity that the first monolayer is completed without second layer nucleation (see Fig. 4a). This implies that we have unlimited interlayer mass transport, $\lambda_1=1$, from the first layer to the substrate, in accordance with the very small step-edge barrier found for the first layer. Since higher layers show almost perfect Poisson distributions (Figs. 5e and 5f), interlayer mass transport from the third and fourth layers can be excluded, i.e. $\lambda_3=\lambda_4=0$. Hence, downward diffusion from the second layer, λ_2, is the only parameter in the following set of differential equations describing the evolution of the film morphology

$$\dot{\Theta}_2=\mathrm{F}[(1-\Theta_2+\lambda_2\Theta_2-\Theta_3)], \tag{2}$$

$$\dot{\Theta}_3=\mathrm{F}(1-\lambda_2)(\Theta_2-\Theta_3), \tag{3}$$

$$\dot{\Theta}_4=\mathrm{F}(\Theta_3-\Theta_4). \tag{4}$$

These equations have been solved analytically with the initial conditions $\Theta_2(t=0)=\alpha$, $\Theta_3(0)=\Theta_4(0)=0$, where α is the fraction of the second layer that grows without nucleation on top. It corresponds to the critical coverage Θ_c for nucleation on top introduced for circular islands in former studies [17,18]. Although α is in principle a second parameter in our model, we would like to point out that the result for λ_2 is quite insensitive to its choice. When we apply this model, for instance, to the growth morphology at 170 K the best fit for λ_2 varies only by $\pm 5\%$ for α from 0 to 0.4 ML; from Fig. 4b it is seen that $\alpha=0.1$ ML is the most realistic choice.

The histogram of uncovered layers for a 1.7 ML film at 200 K calculated with the above model yields best agreement with experiment for $\lambda_2=0.86$ ($\alpha=0.1$ ML) as shown in Fig. 5d. For the 2.1 ML film at 170 K, on the other hand, a fraction of $\lambda_2=0.45$ atoms that can descend after being deposited onto the second layer yields best agreement with the experimental layer occupations from Fig. 4c. Since the film morphologies are not intrinsically different at 170 K and 200 K, it can be assumed that the ratio of these fractions also reflects the ratio of the interlayer diffusion rates at both temperatures, i.e.

$$\frac{\lambda_2(200\ \mathrm{K})}{\lambda_2(170\ \mathrm{K})}\approx\frac{\nu_{200\ \mathrm{K}}}{\nu_{170\ \mathrm{K}}}=\exp\left[\frac{\Delta E_s}{k}\left(\frac{1}{170\ \mathrm{K}}-\frac{1}{200\ \mathrm{K}}\right)\right].$$

From this we obtain an additional barrier for interlayer diffusion from the second to the first Ag layer on Pt(111) of $\Delta E_s=60\pm 20$ meV. The large error bar here is due to the fact that the linear model is a rough approximation since λ is not constant during nucleation and growth of islands, which compete with interlayer diffusion. The barrier for the second monolayer is therefore much less precise than our values for Ag(111) and the first Ag layer, deduced from a full rate equation analysis as described above. It is quite reasonable that the value for the second layer lies between the pseudomorphically strained and the relaxed Ag(111) case. This indicates that there is still some strain effectively facilitating interlayer diffusion.

3.3. Strain relief patterns

At 250 K, the first three Ag monolayers grow almost perfectly layerwise on top of the Pt(111)

surface. This is illustrated in Fig. 6a. The smooth morphology of the third monolayer in Fig. 6a coincides with the appearance of a tiny vertical modulation on the terraces. Meandering pairs of localized dark stripes are detected in the STM images. These stripes represent partial misfit dislocations in which the strain resulting from the lattice mismatch is locally relieved [34]. It is important to notice that for growth temperatures below 250 K the terraces largely appear flat and dislocations are detected with much less density. This can be explained as follows. At low temperatures, the growth of the first layers starts by forming ramified islands of relatively small branch widths attached to the substrate steps. In such islands it is possible to relieve the strain at the island edges without

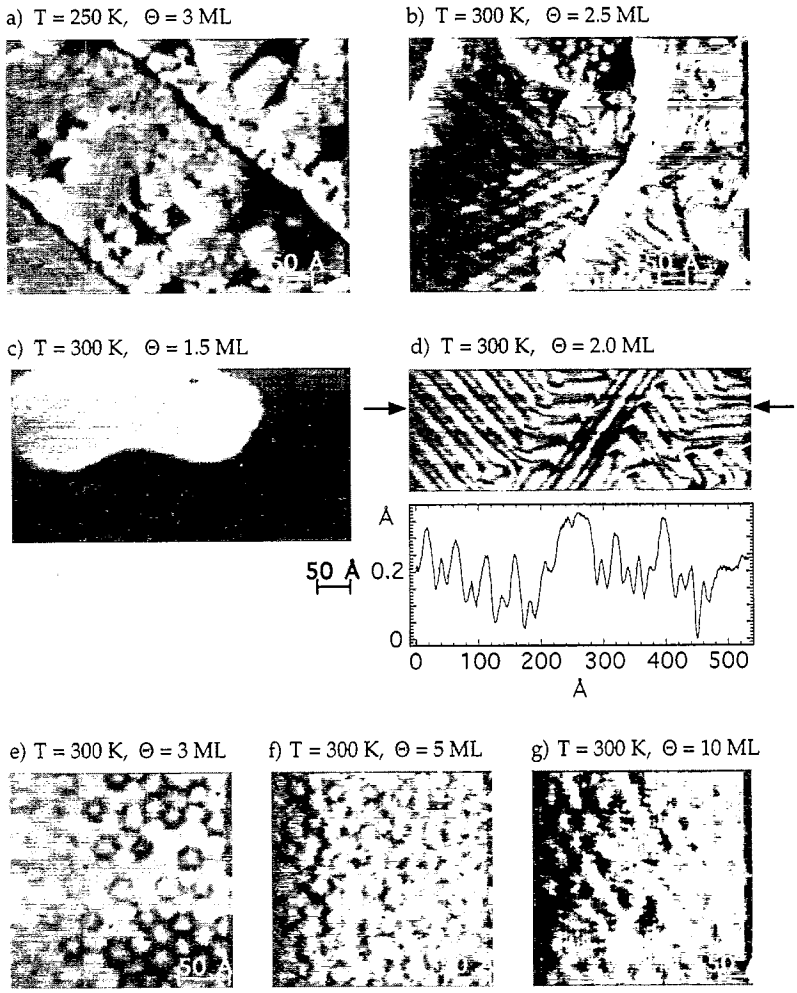

Fig. 6. Strain relief for Ag/Pt(111) as a function of film thickness for films grown around room temperature: (a) 3 ML, 250 K, disordered dislocations; (b) 2.5 ML at 300 K, a striped phase forms on the second layer while the third layer shows a quasi-hexagonal phase; (c) 1.5 ML at 300 K, the completed first layer is pseudomorphic and consequently appears perfectly flat in the STM image whereas the second layer island shows the striped phase; (d) 2.0 ML, 300 K striped phase with line scan showing the inverse imaging of dislocations and the imaging heights of hcp and fcc areas (note that larger hcp areas at the domain boundary appear higher than the narrow stripes with the same stacking within the domain); (e) 3 ML, 300 K quasi-hexagonal phase; (f) 5 ML, 300 K and (g) 10 ML, 300 K weakly modulated moiré-like phases.

formation of dislocations. When the regions between the branches are filled during further growth, the rearrangement of the material into the structure with dislocations is associated with an activation barrier too high to be overcome at temperatures below 250 K. Therefore, at 250 K there is a distinct change in film structure with the occurrence of a high density of dislocations that form rather complex patterns. Since they strongly affect the intralayer mobility, and thus the growth kinetics, we will discuss the various dislocation patterns that form as a function of layer thickness and temperature.

In Fig. 6b we show the misfit dislocations which develop upon growth of a 2.5 ML film at 300 K. The second layer reveals the so-called "striped" weakly incommensurate phase, where strain is relieved anisotropically in one of the $\langle 1\bar{1}0\rangle$-directions per domain by the introduction of a pair of partial misfit dislocations running perpendicular to this direction. Notice that at 250 K this striped phase is present in the third layer (Fig. 6a) whereas at 300 K it characterizes the second layer. At the higher temperature the third layer converts to a structure with quasi-hexagonal symmetry (see Figs. 6b and 6e). This already illustrates the temperature dependence of strain relief due to the activation energy associated with the formation and ordering of misfit dislocations.

The striped phase is in fact quite similar to the $(22\times\sqrt{3})$-reconstruction of Au(111) [46–48] and has also been observed for Cu [49–51] and Ag [52] films on Ru(0001). This structure formed by the second Ag layer on Pt(111) at 300 K is resolved in more detail in the STM data reproduced in Figs. 6c and 6d. Fig. 6c shows a second layer island with partial dislocations that separate brighter imaged areas with two different widths corresponding to fcc and hcp stacking areas. Since the pseudomorphic stacking regions of the Ag layers are under compressive strain, the domain walls in which strain is relieved must represent areas of locally lower density, i.e. they are so called "light" walls. This is opposite to the Au(111) reconstruction and Cu/Ru where the dislocations are areas of locally increased density. Also, in contrast to the Au(111) reconstruction, and to our former interpretation, there are more hcp than fcc sites in this phase, as recently revealed by X-ray photoelectron diffraction [35]. Notice that, in agreement with this finding, in Fig. 6d the narrow areas are imaged lower by 0.09 ± 0.02 Å than the wider ones. This is in accordance with the fact that fcc areas within the Au and Pt reconstruction have been imaged lower than hcp regions by about the same amount (0.08 Å and 0.09 ± 0.02 Å for Au and Pt, respectively) [22,46]. Notice that the striped phase of the second layer is metastable. Upon annealing to $T\geq 700$ K (or growth at $T\geq 500$ K) it converts into the equilibrium structure which is a trigonal network where the partial dislocations cross, allowing for more isotropic strain relief [34]. With this transformation the population of sites also changes in favor of fcc stacking as expected from their generally higher binding energy. Since the subsequent layers grow in fcc stacking with respect to the second layer, the growth or annealing temperature of the second layer determines whether the whole Ag film grows with or without stacking faults with respect to the Pt(111) substrate [35].

In Fig. 6c the tip clearly resolves the dislocations on the second layer while the first layer is imaged flat. This demonstrates that the first layer, when almost completed, is bare of dislocations and hence pseudomorphic [53]. The dislocations on the second layer appear dark in the STM topographs. Since atoms in dislocations are adsorbed on bridge sites this STM contrast is inverted to the geometry expected from a simple ball model.

3.4. STM-imaging of dislocations

There have been reports in recent literature of several metal-on-metal systems where atoms located in dislocations, or even at on-top sites, were imaged "inverted" to their expected geometry by STM. We reported the first such case some years ago [34] for the second Ag layer on Pt(111). At that time we discussed the STM contrast in terms of a strain-related charge density effect that outweighs the variation of geometrical height. According to this argument, the pseudomorphic fcc and hcp areas of Ag/Pt which are under compressive strain should have more charge density and hence appear brighter in STM images then the "light" walls that should appear dark, which is

observed in the STM topographs. In the light of recent literature, and from theoretical calculations performed for the present system, we now take up the discussion of STM contrast in dislocations as well as at Ag seamed substrate steps.

Recently, a striped phase with dislocations also appearing dark to STM has been found for Ag/Ru(0001) which similarly exhibits compressive strain [52]. However, an alternative explanation to our strain argument has been proposed for this contrast. Embedded Atom Method (EAM) calculations showed a buckling of the substrate, notably the first Ru layer underneath the Au adlayer. The buckling is so strong that dislocations, even though involving atoms on bridge sites, are lower than pseudomorphic areas where atoms are located at threefold hollows. The STM contrast can therefore be simply interpreted as geometric height. A geometry inverse to expectation from a hard sphere model has also been found in calculations for moiré structures like Ag/Cu(111) [54,55], as well as in STM experiment and theory for Au/Ni(111) [56] and recently also for Pb/Cu(111) [57]. In these cases on-top sites have the lowest adsorption geometry caused by buckling of the underlying layers.

Motivated by these results we performed calculations for the second Ag layer on Pt(111) within Effective Medium Theory (EMT) [58–60]. For this purpose we used a Pt(111) slab of 30 atoms long, $6/\sqrt{3}$ atoms wide [61] and 20 Pt layers deep, 18 of which were free to relax. Adsorbed on this substrate were two Ag layers, each having two Shockley partial dislocations oriented along $\langle\bar{1}\bar{1}2\rangle$. After energy minimization of this slab, we find a strong buckling of the substrate in agreement with similar calculations for the different systems cited above. In our case, however, the buckling extends up to 15 layers deep. (It was therefore essential for the resulting geometry to contain at least 15 substrate layers that are free to relax). The buckling is such that the Ag atoms of the uppermost layer located in dislocations are lower by 0.11 Å than those on fcc and hcp sites. It can be inferred from the line scan in Fig. 6d that this is very close to the measured difference in apparent height, which amounts to 0.13 ± 0.02 Å between dislocations and hcp areas. This agreement therefore strongly suggests that STM topographs of dislocations can indeed be interpreted as the geometric height and our former interpretation of local variations in atomic density, and the associated variation in total charge density, does not apply to the present case.

It is interesting to analyze the interatomic distances in the uppermost Ag layer obtained from EMT and to compare the results with the reconstructions on Au and Pt(111). It came as a surprise when the first STM images showing the atomic structure of dislocations revealed that for Au(111) the hcp areas have the strongest contraction, followed by fcc areas, whereas atoms in the dislocations are furthest apart [46]. This observation contradicted double soliton models [62] as well as the frequently used description of dislocations as well defined transitions from fcc via bridge to hcp stacking on a rigid substrate. A more adequate description is that a pair of partial dislocations forms a single compression soliton, its center containing the hcp areas where compression is strongest. A recent STM study of the Pt(111) reconstruction also reported strongest contraction for the hcp areas [63], suggesting that this description might generally apply for systems under tensile strain. Ag/Pt, on the other hand, reveals compressive strain and EMT calculations suggest that for that case a double soliton model seems more appropriate. For the slab described above we find that inter-atomic distances in the surface plane are largest (2.5% more than the average distance in the surface) at dislocations and smallest in the fcc and hcp stacking areas (−1.5%). In these calculations dislocations on the second Ag layer on Pt(111) therefore represent areas of locally reduced density. The calculations also show that, although the substrate is strongly involved in the strain variation at the surface, the picture of a transition from fcc to hcp stacking is still valid since the surface atoms are laterally displaced by 1/3 when crossing a partial dislocation.

From the STM image reproduced in Fig. 6d there are two further variations in imaging heights that need to be explained. First, we observe that wider hcp areas (like those located at the domain boundary above the white arrow) are imaged higher than the hcp stripes within the domain (by 0.16 Å, see line scan in Fig. 6d). Second, whenever a pair of partial dislocations ends, they are closed

abruptly by a short partial dislocation running parallel to the close packed rows (see white arrow in Fig. 6d). These dislocations appear by 0.20 Å lower than the longer perpendicular dislocations (atoms are still at bridge sites there, see model for the triangular dislocation network in Ref. [34]). When STM contrast is entirely interpreted as adsorption height, then both observations imply that buckling of the underlying layers must be a very long-range effect thus giving rise to a variety of adsorption heights detectable at the surface. It is, however, not excluded that an electronic, respectively strain effect, as formerly suggested, is contributing to the observed imaging. Both adsorption heights can be explained by such an argument.

Finally we note that the difference in imaging height between the first Ag layer and a Pt step (0.6 Å [34,64]) cannot be accounted for by pure geometry. A similar difference has also been found for Au/Ru(0001) where the first Au layer is under analogous compressive strain [65]. In calculations within EMT for a pseudomorphic Ag seam attached to a Pt(111) step, again including relaxation of 18 underlying layers, we find that Ag surface atoms are adsorbed 0.15 Å higher than those of Pt. This only partly explains the difference in apparent height, therefore suggesting that an electronic effect is contributing to the observed imaging at Ag seamed substrate steps. Since the difference in imaging height is observed to be independent of the tunneling current (excluding work function effects) and voltage (excluding energetic density of states effects), the only reasonable electronic effect is that of the correlation of strain and total charge density. There are indeed strong indications for such a correlation from infrared absorption experiments on differently strained metal layers [66]. Since there is a discontinuity in strain where the pseudomorphic Ag layer is attached to a Pt step this naturally explains the observed imaging.

The difference in imaging height within dislocations of Ag/Pt(111) is presumably due to geometry caused by long-range substrate buckling, whereas the STM contrast at a Ag–Pt hetero-step cannot be accounted for in a pure geometric model. This implies that electronic effects take part in the observed imaging; most probably this would be an effect of strain and total charge density at the surface.

3.5. Strain relief for thicker layers and transition to Ag(111) symmetry

The symmetry of the domain wall pattern changes from uniaxial to quasi-hexagonal for films thicker than 2 ML grown at 300 K. The third monolayer (see Fig. 6b top and Fig. 6e) exhibits a periodic structure consisting of hexagonally arranged protruding areas surrounded by darker lines which again mark well localized partial dislocations. The space between these hexagons is again divided by partial dislocations although these are less clearly visible in the STM topographs. The unit cell of the third layer is a rhombus quite similar to that of the trigonal dislocation pattern characterizing the equilibrium structure of the second layer. Therefore the striped phase of the second layer is unstable towards transformation into a hexagonal dislocation network when it is covered with an additional Ag layer at 300 K.

The hexagonal domain wall network persists up to about 10 ML thick films (see Figs. 6f and 6g). Notice, however, the decrease in image contrast at 10 ML, which is associated with less well localized domain walls, indicating a transition to a moiré-like phase. Thicker films transform into a weakly modulated structure with the Ag(111) interplanar lattice constant. This transition in film structure from a misfit dislocation network to a weakly modulated incommensurate structure has also been detected in high resolution He-diffraction measurements [43,67]. Up to 9–10 ML the diffraction spectra show a splitting of the (0,1) diffraction beam characteristic for a dislocation network with its (1×1) pseudomorphic domains and the localized strain relief in narrow domain walls of lower density. At a Ag film thickness above 10 ML no splitting of the (0,1) diffraction peak is detectable; only one diffraction peak, corresponding to an interplanar lattice constant of 2.89 Å, is measured indicating the growth of Ag layers with bulk Ag(111) structure.

As in the cases of lower growth temperatures, at 300 K the structural transition from a domain wall phase to an incommensurate Ag(111) phase (with

essentially bulk lattice constant) is also accompanied by a change in growth mode. This is illustrated in Fig. 7. While up to about 6–9 ML the Ag film grows two-dimensionally at 300 K, above that critical coverage the film grows in a 3D mode. At the nominal coverages of 3, 6 and 9 ML only 2 layers are uncovered (pin holes will be discussed below) indicating an ideal layer-by-layer growth. Films thicker than 10 ML grow in a rough three-dimensional mode. This is demonstrated for the case of a 25 ML film by the STM image in Fig. 7d. Growth pyramids have developed and 14 monolayers are found to be exposed simultaneously. This morphology is identical to the one observed by Meyer et al. for Ag(111) homoepitaxy at room temperature [15] which corroborates the transition to Ag(111) symmetry for Ag films thicker than 10 ML grown on Pt(111) at room temperature.

3.6. Formation of pin holes at former substrate steps

The presence of pin holes is evident from inspection of Fig. 7c. They can be up to 6 ML deep and thus considerably disrupt the 2D quality of the film. Such pin holes can substantially disturb the physical properties of thin films, e.g. in magnetic multilayers where the anti-ferromagnetic interlayer

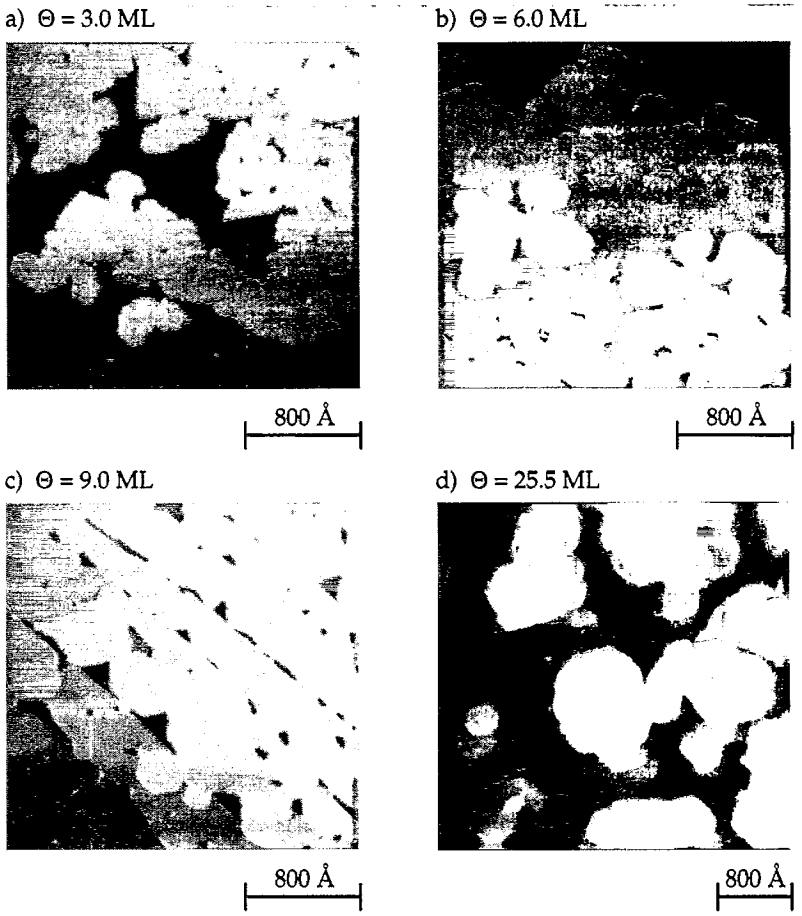

Fig. 7. Growth scenario of Ag heteroepitaxy on Pt(111) at 300 K; the growth mode changes from 2D to 3D above a critical coverage of 10 ML. The STM images characterize the morphology of (a) 3 ML (notice the former substrate steps), (b) 6 ML, (c) 9 ML (notice the pin holes located at the former substrate steps) and (d) 25.5 ML thick Ag films.

exchange coupling can be hampered by ferromagnetic bridges through pin holes in the spacer layer [68]. To avoid such effects it is of fundamental importance to understand the mechanism by which pin holes form. For the present system we can analyze their origin from inspection of the island shapes close to substrate steps. Fig. 8a shows a particularly interesting case, where 1.1 ML have been deposited at 200 K such that the substrate steps are wetted by the pseudomorphic Ag layer. Islands that approach these steps from the Pt side are bending and apparently not able to grow over this 2D Ag–Pt border. On the other hand, atoms that approach this border from the Ag side must also encounter a repulsive potential since, first, the former step acts as a nucleation site for second layer islands and, second, these islands grow exclusively away from the substrate step. Both these effects are clearly seen from the elongated second layer island in Fig. 4b (1.1 ML, 170 K). Its location is directly at the lateral Ag–Pt interface and growth is restricted to the Ag terrace to its left whereas the small Pt patch to its right remains bare of Ag. The repulsive effects from both sides of the Ag–Pt interface are illustrated together with an intuitive potential in the upper part of Fig. 8b. Notice that the repulsion when coming from the Pt side can be rationalized by the upward step in potential mentioned above which reflects the lower binding energy (by 170 meV) for a Ag atom on the first Ag layer compared to that on Pt(111) [33]. It is a very interesting effect, however, that atoms are repelled when traveling from Ag to Pt, even though gaining binding energy in being bound to Pt. It was shown above that a Ag adatom has almost no barrier to descend from an isolated Ag island adsorbed on a Pt terrace. There we argued that strain is relieved at edges thus facilitating downward diffusion by exchange. In the particular case of the Ag–Pt interface the Ag layer is under constraint apparently leading to a significant barrier for diffusion onto the adjacent Pt terrace.

It is evident that both these repulsions lead to the formation of troughs located at the substrate steps (see fig. 6a); material landing on the Ag terraces below is all incorporated into second layer islands which exclusively grow away from the former step; on the other hand, the material landing on the upper Ag terrace is mostly incorporated into growing islands and only a very small amount

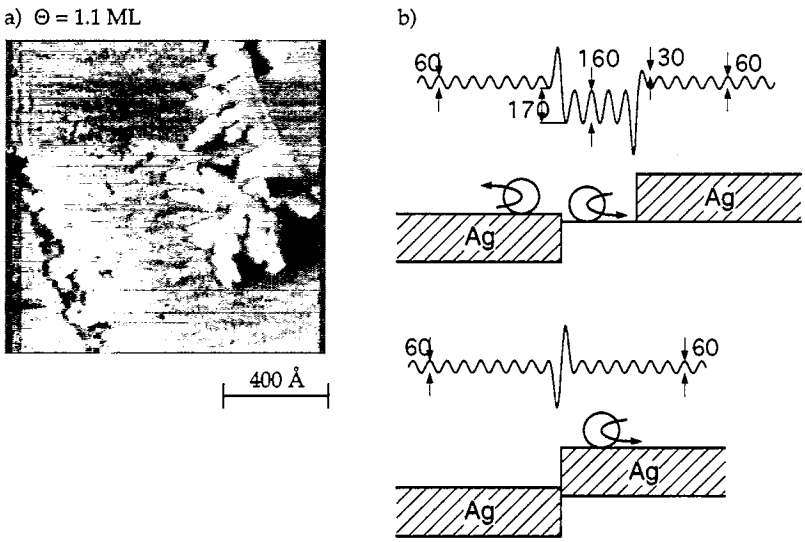

Fig. 8. (a) The morphology of a 1.1 ML Ag film grown at 200 K uncovers some peculiarities of the potential for Ag adatoms approaching a Ag wetted Pt step; (b) schematic drawings showing in which situations Ag adatoms are reflected at heterogeneous Ag–Pt or Ag–Ag steps. Above each of them there is a suggested interaction potential, where the measured corrugations are indicated (units: meV).

can descend to fill the remaining holes close to the steps. We might now ask how this effect can persist to higher layers. The fact that developing first layer islands are hindered from passing the Ag–Pt interfaces not only imples that atoms approaching this interface must be reflected; it also indicates that atoms diffusing on top of the first layer must be hampered from descending when reaching the step directly located above the Ag–Pt interface, since otherwise the island would have a way to pass this interface. Therefore the otherwise very low barrier to interlayer diffusion from the first layer is now seen to be significant. This strongly supports the strain argument given above for the low barrier on free islands. At the former Pt step the Ag layer cannot relax laterally, so descent by exchange is inhibited. Hence the atom has to diffuse downward in the classical way, which is associated with a significantly higher barrier. This is illustrated schematically in the intuitive picture at the bottom of Fig. 8b.

The second layer exhibits similar repulsive barriers hindering the islands from passing former step edges as, for example, demonstrated in Fig. 4c. The amount of material lacking to fill the troughs at the substrate steps is quite small. It results from the concurrence of growing islands and the particular form of the potential at Ag–Pt and Ag–Ag interfaces located at the former substrate steps. For thicker films, this leads to the formation of narrow, deep troughs located at former substrate steps. These pin holes are even present in the 9 ML thick film which shows the remarkably long range of this effect.

3.7. *Transition to 3D growth and Ag(111) structure*

The correlation between the change in growth mode from 2D to 3D and the transition in film structure from a strained to an incommensurate Ag(111) structure (essentially relaxed and strain free) holds in the entire kinetic growth regime below 300 K. At temperatures below 170 K the film structure changes directly from a pseudomorphic layer to Ag bulk-like crystallites immediately after completion of the first monolayer. At 200 K the transition from 2D to 3D growth occurs after the second monolayer. This is exactly the temperature at which the second monolayer is found to show the first indications of partial strain relief through misfit dislocations while Ag in the third monolayer basically crystallizes with bulk structure. With increasing temperature the layer thickness for the transition from partially strained (domain wall phase) to unstrained Ag(111) increases through 3 ML at 250 K to 6–9 ML at 300 K; this change in structure is always accompanied by a corresponding change in growth morphology from 2D to 3D. The reason for this change is of solely kinetic origin. It is essentially due to the fact that compressive strain reduces the additional barrier at steps, presumably because it facilitates interlayer diffusion by exchange. As long as the film shows dislocations there are strained areas where interlayer diffusion is promoted. These areas disappear when the transition to Ag crystal structure takes place; from there on interlayer diffusion is associated with a high activation energy which cannot be overcome sufficiently frequently at temperatures below 400 K, leading to 3D growth.

The 3D growth beyond a certain number of layers is thus distinctively different from the thermodynamic Stranski–Krastanov mode. It should be noted that whenever this system is not under kinetic limitations it grows 2D, i.e. at any coverage perfectly flat layers can be grown when deposited at, or annealed to, sufficiently high temperatures. This is in agreement with the large negative surface free energy difference $\gamma_{Ag(111)}-\gamma_{Pt(111)} \approx -0.5$ eV atom^{-1}. This difference is based on the theoretical values available, i.e. $\gamma_{Ag(111)}=0.55$ eV atom^{-1} [69] and $\gamma_{Pt(111)}=1.05$ eV atom^{-1} [70]. Experimental values exist only for average surface orientations but they are quite close to the theoretical values, when recalculated to the (111) atomic density, i.e. $\gamma_{Ag}=0.57$ eV atom^{-1} and $\gamma_{Pt}=1.06$ eV atom^{-1} [71,72]. At deposition temperatures above $\sim$450 K the additional step-edge barrier of 120 meV of relaxed Ag(111) can be overcome. A 25 ML thick film grown at 450 K is shown in Fig. 9a. It is flat apart from some pin holes that persist indicating that the barriers discussed above located at the former substrate steps are still effective at this temperature. Upon deposition of the same amount at 600 K and subsequent annealing to 800 K eventually this barrier can also be overcome and a perfectly flat

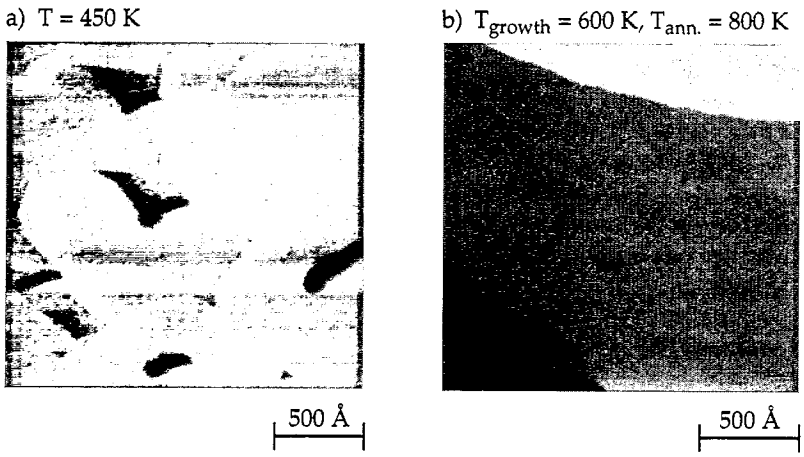

Fig. 9. A 25 ML thick Ag film grown at 450 K is flat apart from a few pin holes located at former substrate steps (a), these disappear upon growth of the same amount at 600 K and annealing to 800 K, leading to a perfectly flat Ag film with the Ag(111) lattice constant (b).

Ag(111) single crystal surface results as illustrated in Fig. 9b.

4. Conclusion

We have observed strain-mediated two-dimensional growth in Ag heteroepitaxy on Pt(111). The barrier for adatoms descending a step edge is lowered through the edge-relaxation of strained Ag islands enhancing the interlayer mass transport and driving the system towards 2D growth. The additional step edge barrier ΔE_s of the fully strained pseudomorphic monolayer has been determined to be only 25% of the barrier of the relaxed Ag(111) layer; the reduction of the barrier of the partially strained second monolayer was found to be still of the order of 50% with respect to the relaxed Ag(111) bulk surface. This shows the significant effect of strain on interlayer diffusion. The thickness at which the film adopts the Ag(111) lattice constant is temperature dependent through the activation energy associated with the formation of dislocations. Thus, the layer-dependent transition to 3D growth of the Ag/Pt(111) system can be explained by the fact that a "strain-free" Ag(111) surface has a non-negligible barrier for interlayer mass transport, while strained or partially strained Ag layers have a substantially reduced barrier. Moreover, we have recently demonstrated that strain also effects the intralayer mass transport. A compressively strained surface has a lowered diffusion barrier while a surface under tensile strain has a higher barrier with respect to the unstrained surface.

There is a strong repulsive barrier located at former substrate steps which persists up to thick layers. It is the origin for pin holes that can be several layers deep and significantly affect the film quality.

The strain dependent inter- and intralayer diffusion is of general importance for heteroepitaxial growth with significant structural misfit. A proper account of strain effects requires in new concepts of layer-dependent nucleation kinetics for heteroepitaxial systems. In addition, strain relief has been found to be strongly temperature dependent which significantly complicates proper modeling of heteroepitaxial systems. On the other hand, the strong dependence of nucleation kinetics on strain and the dislocation patterns associated with its relief can be exploited to influence growth morphologies and nucleation densities.

Acknowledgement

We gratefully acknowledge experimental contributions from M. Giovannini and valuable discus-

sions with J.V. Barth. We are also grateful to the group of Prof. J. Nørskov for providing us with the EMT code. This research has been supported by the Schweizerischer Nationalfonds.

References

[1] E. Bauer, Z. Kristallogr. 110 (1958) 372.
[2] E. Bauer and H.J.v.d. Merwe, Phys. Rev. B 33 (1986) 3657.
[3] G.L. Lay and R. Kern, J. Cryst. Growth 44 (1978) 197.
[4] J.A. Venables, G.D.T. Spiller and M. Hanbücken, Rep. Prog. Phys. 47 (1984) 399.
[5] C. Ratsch and A. Zangwill, Surf. Sci. 293 (1993) 123.
[6] G.L. Price, Appl. Phys. Lett. 53 (1988) 1288.
[7] J.H.v.d. Merwe, D.L. Tönsing and P.M. Stoop, Surf. Sci. 312 (1994) 387.
[8] G. Ehrlich and F.G. Hudda, J. Chem. Phys. 44 (1966) 1039.
[9] R.L. Schwoebel and E.J. Shipsey, J. Appl. Phys. 37 (1966) 3682.
[10] R.L. Schwoebel, J. Appl. Phys. 40 (1969) 614.
[11] Notice that the periodic appearance of a reconstruction can significantly alter successive diffusivities, as in the case of Pt(111) discussed below.
[12] These arguments only hold for low index surface planes which have low surface free energies. On higher index planes faceting might be thermodynamically favored.
[13] H.A. v.d. Vegt, H.M. v. Pinxteren, M. Lohmeier, E. Vlieg and J.M. Thornton, Phys. Rev. Lett. 68 (1992) 3335.
[14] G. Rosenfeld, R. Servaty, C. Teichert, B. Poelsema and G. Comsa, Phys. Rev. Lett. 71 (1993) 895.
[15] J. Vrijmoeth, H.A.v.d. Vegt, J.A. Meyer, E. Vlieg and R.J. Behm, Phys. Rev. Lett. 72 (1994) 3843.
[16] K. Bromann, H. Brune, H. Röder and K. Kern, Phys. Rev. Lett. 75 (1995) 677.
[17] J.A. Meyer, J. Vrijmoeth, H.A. v.d. Vegt, E. Vlieg and R.J. Behm, Phys. Rev. B 51 (1995) 14790.
[18] P. Smilauer and S. Harris, Phys. Rev. B 51 (1995) 14798.
[19] R. Kunkel, B. Poelsema, L.K. Verheij and G. Comsa, Phys. Rev. Lett. 65 (1990) 733.
[20] J. Jacobsen, K.W. Jacobsen, P. Stoltze and J.K. Nørskov, Phys. Rev. Lett. 74 (1995) 2295.
[21] T. Michely, M. Hohage, S. Esch and G. Comsa, Surf. Sci. 349 (1996) L89.
[22] M. Bott, M. Hohage, T. Michely and G. Comsa, Phys. Rev. Lett. 70 (1993) 1489.
[23] G. Rosenfeld, B. Poelsema and G. Comsa, J. Cryst. Growth 151 (1995) 230.
[24] H. Brune, K. Bromann, H. Röder, K. Kern, J. Jacobsen, P. Stolze, K. Jacobsen and J. Nørskov, Phys. Rev. B 52 (1995) R14380.
[25] J.A. Meyer, P. Schmid and R.J. Behm, Phys. Rev. Lett. 74 (1995) 3864.
[26] H. Röder, H. Brune, J.P. Bucher and K. Kern, Surf. Sci. 298 (1993) 121.
[27] H. Brune, H. Röder, K. Bromann and K. Kern, Thin Solid Films 264 (1995) 230.
[28] To be more precise, the z signal is high-passed (30 Hz, first order) before being recorded. Therefore an ascending step is followed by a bright seam with a certain width (small islands therefore appear entirely bright) and descending steps have a black seam to their right which appears to be the island's shadow.
[29] H. Brune, C. Romainczyk, H. Röder and K. Kern, Nature 369 (1994) 469.
[30] H. Röder, K. Bromann, H. Brune and K. Kern, Phys. Rev. Lett. 74 (1995) 3217.
[31] H. Brune, K. Bromann, J. Jacobsen, K. Jacobsen, P. Stoltze, J. Nørskov and K. Kern, Surf. Sci. 349 (1996) L115.
[32] H. Brune, H. Röder, C. Boragno and K. Kern, Phys. Rev. Lett. 73 (1994) 1955.
[33] T. Härtel, U. Strüber and J. Küppers, Thin Solid Films 229 (1993) 163.
[34] H. Brune, H. Röder, C. Boragno and K. Kern, Phys. Rev. B 49 (1994) 2997.
[35] G. Rangelov, T. Fauster, U. Strüber and J. Küppers, Surf. Sci. 331–333 (1995) 948.
[36] C. Ratsch, A.P. Seitsonen and M. Scheffler, to be published.
[37] J.J. Mortensen, B. Hammer, O.H. Nielsen, K.W. Jacobsen and J.K. Nørskov, in: Solid State Sciences Series, Vol. 121, Ed. A. Okiji (Springer, Berlin, 1996).
[38] J. Tersoff, A.W.D.v.d. Gon and R.M. Tromp, Phys. Rev. Lett. 72 (1994) 266.
[39] D. Stauffer and A. Aharony, Introduction to Percolation Theory (Taylor and Francis, London, 1992).
[40] P. Smilauer, Contemp. Phys. 32 (1991) 89.
[41] R. Stumpf and M. Scheffler, Phys. Rev. Lett. 72 (1994) 254.
[42] Y. Li and A.E. DePristo, Surf. Sci. 319 (1994) 141.
[43] C. Romainczyk, Ph.D. thesis, Ecole Polytechnique Fédérale de Lausanne, Switzerland, 1994.
[44] C. Günther, S. Günther, E. Kopatzki, R.Q. Hwang, J. Schröder, J. Vrijmoeth and R.J. Behm, Ber. Bunsenges. Phys. Chem. 97 (1993) 522.
[45] P.I. Cohen, G.S. Petrich, P.R. Pukite and G.J. Whaley, Surf. Sci. 216 (1989) 222.
[46] J.V. Barth, H. Brune, G. Ertl and R.J. Behm, Phys. Rev. B 42 (1990) 9307.
[47] Y. Tanishiro, H. Kanamori, K. Takayanagi, K. Yagi and G. Honjo, Surf. Sci. 111 (1981) 395.
[48] C. Wöll, S. Chiang, R.J. Wilson and P.H. Lippel, Phys. Rev. B 39 (1989) 7988.
[49] G.O. Pötschke and R.J. Behm, Phys. Rev. B 44 (1991) 1442.
[50] C. Günther, J. Vrijmoeth, R.Q. Hwang and R.J. Behm, Phys. Rev. Lett. 74 (1995) 754.
[51] J.C. Hamilton and S.M. Foiles, Phys. Rev. Lett. 75 (1995) 882.

[52] R.Q. Hwang, J.C. Hamilton, J.L. Stevens and S.M. Foiles, Phys. Rev. Lett. 75 (1995) 4242.
[53] First monolayer Ag islands grown at room temperature or above on Pt(111) also show dislocations. Interestingly, these dislocations disappear upon completion of the first layer. We will address this surprising finding in detail in a forthcoming publication.
[54] C. Mottet, G. Tréglia and B. Legrand, Phys. Rev. B 46 (1992) 16018.
[55] S.M. Foiles, Surf. Sci. 292 (1993) 5.
[56] J. Jacobsen, L.P. Nielsen, F. Besenbacher, I. Stensgaard, E. Lægsgaard, T. Rasmussen, K.W. Jacobsen and J.K. Nørskov, Phys. Rev. Lett. 75 (1995) 489.
[57] C. Nagl, M. Schmid and P. Varga, to be published.
[58] P. Stoltze, J. Phys. Condens. Matter 6 (1994) 9495.
[59] K.W. Jacobsen, Comments Cond. Mat. Phys. 14 (1988) 129.
[60] J.K. Nørskov, K.W. Jacobsen, P. Stoltze and L.B. Hansen, Surf. Sci. 283 (1993) 277.
[61] We used Cartesian coordinates in the surface plane to obtain periodic boundary conditions in the direction of the dislocations.
[62] U. Harten, A.M. Lahee, J.P. Toennies and C. Wöll, Phys. Rev. Lett. 54 (1985) 2619.
[63] M. Hohage, T. Michely and G. Comsa, Surf. Sci. 337 (1995) 249.
[64] H. Röder, R. Schuster, H. Brune and K. Kern, Phys. Rev. Lett. 71 (1993) 2086.
[65] J. Schröder, C. Günther, R.Q. Hwang and R.J. Behm, Ultramicroscopy 42–44 (1992) 475.
[66] E. Kampshoff, E. Hahn and K. Kern, Phys. Rev. Lett. 73 (1994) 704.
[67] H. Brune and K. Kern, in: The Chemical Physics of Solid Surfaces, Vol. 8, Eds. D.A. King and D.P. Woodruff (1996).
[68] R. Coehoorn, Europhys. News 24 (1993) 43.
[69] M. Methfessel, D. Henning and M. Scheffler, Phys. Rev. B 46 (1992) 4816.
[70] M.C. Payne, N. Roberts, R.J. Needs, M. Needels and J.D. Jeannopoulos, Surf. Sci. 211/212 (1989) 1.
[71] A.R. Miedema, Z. Metallkd. 69 (1978) 287.
[72] W.R. Tyson and W.A. Miller, Surf. Sci. 62 (1977) 267.